Atmos. Chem. Phys. Discuss., 14, 14599–14635, 2014
www.atmos-chem-phys-discuss.net/14/14599/2014/
doi:10.5194/acpd-14-14599-2014

Atmospheric Chemistry and Physics Discussions

Arctic low-level boundary layer clouds: in-situ measurements and simulations of mono- and bimodal supercooled droplet size distributions at the cloud top layer

M. Klingebiel[1], A. de Lozar[2], S. Molleker[3], R. Weigel[1], A. Roth[3], L. Schmidt[4], J. Meyer[5,6], A. Ehrlich[7], R. Neuber[4], M. Wendisch[7], and S. Borrmann[1,3]

[1]Institute for Physics of the Atmosphere, University of Mainz, Mainz, Germany
[2]Max Planck Institute for Meteorology, Hamburg, Germany
[3]Max Planck Institute for Chemistry, Mainz, Germany
[4]Alfred Wegener Institute for Polar and Marine Research, Potsdam, Germany
[5]Institut für Energie- und Klimaforschung (IEK-7), Forschungszentrum Jülich, Jülich, Germany
[6]Institute of Energy & Environmental Technology e.V. (IUTA), Duisburg, Germany
[7]Leipzig Institute for Meteorology, University of Leipzig, Leipzig, Germany

Received: 15 April 2014 – Accepted: 19 May 2014 – Published: 5 June 2014

Correspondence to: M. Klingebiel (klingebi@uni-mainz.de)

Published by Copernicus Publications on behalf of the European Geosciences Union.

Abstract

Aircraft borne optical in-situ size distribution measurements were performed within Arctic boundary layer clouds, with a special emphasis on the cloud top layer, during the **VER**tical **D**istribution of **I**ce in Arctic Clouds (VERDI) campaign. The observations were carried out within a joint research activity of seven German institutes to investigate Arctic boundary layer-, mixed-phase clouds in April and May 2012. An instrumented Basler BT-67 research aircraft operated out of Inuvik over the Mackenzie River delta and the Beaufort Sea in the Northwest Territories of Canada. Besides the cloud particle and hydrometeor size spectrometers the aircraft was equipped with instrumentation for aerosol, radiation and other parameters. Inside the cloud, droplet size distributions with monomodal shapes were observed for predominantly liquid-phase Arctic stratocumulus. With increasing altitude inside the cloud the droplet mean diameters grew from 10 µm to 20 µm. In the upper transition zone (i.e. adjacent to the cloud-free air aloft) changes from monomodal to bimodal droplet size distributions were observed. It is shown that droplets of both modes co-exist in the same (small) air volume and the bimodal shape of the measured size distributions cannot be explained as an observational artifact caused by accumulating two droplet populations from different air volumes. The formation of a second size mode can be explained by (a) entrainment and activation/condensation of fresh aerosol particles, or (b) by differential evaporation processes occurring with cloud droplets engulfed in different eddies. Activation of entrained particles seemed a viable possibility as a layer of dry Arctic enhanced background aerosol was detected directly above the stratus cloud might form a second mode of small cloud droplets. However, theoretical considerations and a model simulation revealed that, instead, turbulent mixing and evaporation of larger droplets most likely are the main reasons for the formation of the second droplet size mode in the uppermost region of the clouds.

1 Introduction

The Arctic sea ice plays an important role in the global climate system as it covers and insulates the Arctic ocean especially in the Winter season and diminishes the exchange of heat, momentum and gases between ocean and atmosphere (Lemke et al., 2007). Surface temperature analyses show the strongest temperature increase in the Arctic region in the past decades between 1961–1971 and 2003–2013 as resulting from the GISS data base (Hansen et al., 2010). This temperature rise drives a melting process of Arctic sea ice which reduces the albedo and, thus, increases absorption of solar radiation at the sea surface, with the consequence of even more enhanced ice melting. This so-called "direct albedo feedback" occurs in the Arctic summer and is a self-amplifying melting effect. As a result the temperature of the upper mixing layer of the Arctic Ocean rises as well. Most of the heat stored during summer in the mixing layer is released in winter leading to an indirect albedo feedback causing Arctic amplification of near-air surface temperature (Wendisch et al., 2013). Satellite measurements (CALIPSO and ICESat) between 2003 and 2008 showed that cloud cover and optical depth reach a maximum over ice-free waters in the Arctic (Palm et al., 2010). The authors also conclude that the higher optical depths are caused by geometrically thicker low level clouds over the water. In addition an increasing trend of cloud coverage between 7 % and 10 % was observed from the satellite instruments most likely as result of decreasing sea ice coverage (Palm et al., 2010). Several publications indicate that Arctic clouds have been influential in recent dramatic Arctic sea ice loss (Kay et al., 2008; Perovich et al., 2008; Schweiger and Lindsay, 2008). The microphysical characteristics of clouds, e.g., particle phase, size, number concentration, and shape determine the radiative properties which influence the atmospheric radiation budget (Curry et al., 1996; Ehrlich et al., 2008a). On the other hand climate simulations indicate that the sea salt emissions may increase with receding ice coverage leading to growing optical depths of the natural background aerosol which implies a negative direct climate forcing of -0.2 to $-0.4\,\mathrm{W\,m^{-2}}$ (Struthers et al., 2011). Such estimates are still highly

uncertain because of the crude representation of Arctic clouds and aerosol-cloud interactions in the model (Struthers et al., 2011) and especially mixed-phase low level clouds are of major concern here. Phase-dependent microphysical processes such as collision, coalescence, aggregation, riming and secondary ice formation processes (e.g., Hallett-Mossop ice multiplication) determine the growth and shape characteristics of the ice particles in mixed-phase Arctic clouds (Pruppacher and Klett, 2010). Nucleation, growth, and sedimentation processes of ice crystals are still not comprehensively understood which leads to discrepancies between observed and expected ice number concentrations from simulations (Fan et al., 2009; Morrison et al., 2008; Avramov et al., 2011).

For the development process of clouds, aerosol particles play a significant role as they provide Cloud Condensation Nuclei (CCN) and influence the direct and indirect radiative effects (Lemke et al., 2007). Many of the previous measurements indicate a correlation between the number concentrations of aerosol and of cloud particles which might imply an influence of aerosol particles on the cloud particle size distribution (SD) (Pruppacher and Klett, 2010). Aerosol particles could also influence the lifetime of clouds which form at the bottom of stable boundary layers (Stevens, 2005). These boundary layer clouds act to cool the atmosphere when averaging their radiative effects annually and globally. Such cooling is due to the dominance of the solar albedo effect as compared with the less important emission of thermal-infrared radiation. However, in the Arctic, boundary layer clouds mostly warm the below-cloud atmosphere. This is due to the generally low sun elevation, the long-lasting polar night, and the high solar surface albedo of land/sea ice and snow (Wendisch et al., 2013; Shupe and Intieri, 2004). Moreover, the magnitude of the radiative forcing of boundary-layer, mixed-phase Arctic clouds also critically depends on the clouds macroscopic and microscopic properties. Therefore, in-situ measurements are necessary to study aerosol-cloud interactions and their radiative effects (Lawson et al., 2001; Lihavainen et al., 2010).

With regard to the cloud radiative effects, the upper top layer of boundary layer clouds is very important because it dominated the overall cloud radiative properties (Ehrlich

et al., 2009) and thus is a key for the Arctic radiation balance (Stevens, 2005). Platnick (2000) showed that for inhomogeneous liquid water clouds the vertical weighting function of the reflected radiation has a maximum at the cloud top. For mixed-phase clouds Ehrlich et al. (2009) showed that a small fraction of ice crystals in the cloud top layer may change the cloud top reflectivity significantly what may also has consequences for the accuracy of cloud remote sensing. Therefore, microphysical processes at cloud top such as the cloud top entrainment are further critical issue which still needs proper representation in the numerical models. Cloud top entrainment is driven by the evaporation at the cloud top inducing downward directed turbulent motion which then entrains the cloud free air above. And this is crucial for the lifetime of the entire cloud as well as the radiative budget because the entrainment and its rates influence directly droplet size and thus reflectivity in the visible. The main sources to produce turbulent energy at the cloud top are radiative cooling and evaporative cooling (Pettersen, 1938; Siems and Bretheron, 1992).

In the past 20 years several aircraft campaigns were conducted to study the properties of arctic clouds:

- In April 2008 the NASA Arctic Research of the Composition of the Troposphere from Aircraft and Satellites (ARCTAS) mission was conducted to better understand the changes in Arctic atmospheric chemical composition and climate (Jacob et al., 2010).
- One year earlier, the Arctic Study of Aerosol, Clouds and Radiation (ASTAR 2007) campaign was performed to characterize microphysical and optical properties of arctic clouds. The thermodynamic phase of the detected clouds was estimated by measurements of the reflected solar radiation. Three different methods were used to identify the ice phase in Arctic boundary layer clouds (Ehrlich et al., 2008b).
- Two earlier campaigns were the Surface Heat Budget of the Arctic (SHEBA) (Perovich et al., 2000), and the

- First ISCCP (International Satellite Cloud Climatology Project) Regional Experiment Arctic Clouds Experiment (FIRE ACE) (Curry et al., 1999).

The SHEBA campaign was conducted 1997–1998 to study the heat transfer processes between the ice covered Arctic Ocean and the atmosphere. At the same time, in April–July 1998, the FIRE ACE campaign was performed to improve (a) the satellite retrieval of cloud and surface characteristics in the Arctic, and (b) the representation of Arctic clouds and radiation in general circulation models. For this purpose, four aircraft were equipped with instrumentation as described in Curry et al. (1999). During FIRE ACE, cloud particle SDs of Arctic boundary layer clouds were studied. Monomodal SDs were mostly observed under adiabatic and homogeneous liquid water cloud conditions whereas bimodal SDs appeared near the cloud top, when the temperature and liquid water content profiles indicated non-adiabatic and inhomogeneous cloud conditions (Lawson et al., 2001). Mixed-phase clouds, which consist of liquid and ice phase particles, appear mainly in the autumn and springtime. Boundary layer clouds containing ice and liquid water were typically detected in May in an altitude range from 150 to 1200 m (Lawson et al., 2001). The detected ice particles usually have diameters between 8 µm and 1 mm while liquid cloud droplets mostly are in a size range of micrometers with maximum droplet number concentrations (N) of 500 cm^{-3} (Curry et al., 1996).

The purpose of this study is to analyze in further detail the microphysical properties inside and at the top of the boundary layer stratus clouds in the Beaufort Sea area with emphasis on the occurrence of monomodal and bimodal distributions and the connection to turbulent mixing processes at the cloud top levels.

2 Field campaign and instrumentation

Airborne microphysical measurements within Arctic boundary layer, mixed-phase clouds were performed during the **VER**tical **D**istribution of **I**ce in Arctic Clouds (VERDI) field campaign. The POLAR 5 research aircraft (the Basler BT-67 modification of a DC-

3), operated by the Alfred Wegener Institute (AWI, Helmholtz Centre for Polar and Marine Research, Bremerhaven, Germany), was equipped with instruments to carry out in-situ measurements aiming, in particular, at mixed-phase clouds, during the Arctic spring season. Four cloud particle spectrometers with partially overlapping detection size ranges were simultaneously operated side by side for providing independent size distribution (SD) measurements. Solar (spectral and broadband) as well as broadband thermal-infrared radiation sensors and an optical particle counter were deployed on the aircraft. Also, a cloud-aerosol LiDAR, and meteorological instruments were part of the instrumentation. With this equipment, different situations of ice-, liquid-phase and mixed phase clouds were probed. VERDI was performed from 25 April to 17 May 2012 out of Inuvik, Canadian Northwest Territories, with the main operation area over the Mackenzie River delta and the Beaufort Sea.

The measurements in this study are mainly based on the Cloud Combination Probe (CCP), the Optical Particle Counter (Sky-OPC), and the LiDAR instrument. The CCP integrates two instruments to measure parameters of individual cloud hydrometeors (Wendisch and Brenquier, 2013) and was a modified version of the instrument initially manufactured by Droplet Measurement Technologies (DMT, Boulder, CO, USA, see http://dropletmeasurement.com/). It consists of a Cloud Droplet Probe (CDP) and a Cloud Imaging Probe (CIP grey scale – denoted as CIPgs in the following) which in combination cover a size diameter range from 2 µm to 960 µm, including large aerosol particles, liquid cloud droplets and small frozen hydrometeors. The technique of the CDP is based on forward light-scattering with a light collection angle from 4° up to 12°, similar to the Forward Scattering Spectrometer Probe (FSSP). A laser diode wavelength of 658 nm is used as light source. The CDP instrument measures particles in a diameter size region between 2 µm and 50 µm with a size resolution provided by 30 detector channels. Its general performance and the sample area were tested and measured using a piezoelectric droplet generator laboratory setup similar to the design of Lance et al. (2010). As a result a sampling area of $0.27 \pm 0.025\,\mathrm{mm}^2$ was obtained. Forward light scattering probes have the disadvantage of often being affected

by shattering (Jensen et al., 2009; Korolev et al., 2011). However, this CDP is an open path design and is equipped with tips of particular shape to minimize the impact of shattering on the measurement. Furthermore, the instrument records the particle-by-particle (PbP) data which allows for excluding collection periods potentially affected by shattering. The CIPgs instrument, the second sub-instrument of the CCP, records two-dimensional shadow images of cloud particles in a size range from 15 µm up to 960 µm with an optical resolution of 15 µm. Specialized algorithms are used to process and analyze the captured images in order to estimate particle number concentrations, particle SDs, and to differentiate particle shapes (Korolev, 2007).

The Sky-OPC is a Series 1.129 aerosol spectrometer manufactured by Grimm Aerosol Technik GmbH (see http://www.grimm-aerosol.com/en/). The Sky-OPC determines the aerosol particle number concentrations within 31 size channels and the particle sizes from 250 nm up to 32 µm. Based on the sampling inlet efficiency of the applied (solid diffuser) aerosol inlet (Huebert et al., 2004) for the POLAR 5 only aerosol particles of up to 1 µm in diameter are representatively sampled from the ambient air. Individual particles are detected by their light scattering signal within an angular range from 60 to 120 ° of a diode-laser with a wavelength of 655 nm. The standard integration time of the Sky-OPC for one SD has been set to 6 s for the VERDI flights. Particle SDs recorded by several in-situ instruments show a good agreement in the overlapping size ranges between 250 nm and 6.4 mm.

The Airborne Mobile Aerosol LiDAR (AMALi) emits laser pulses into the atmosphere and measures backscatter from air molecules and aerosols at the wavelengts 532 nm and 355 nm, as well as depolarization at 532 nm. Here the measurement at 532 nm is used to characterize the spatial structure of aerosol and cloud layers. During VERDI AMALi was operated in nadir pointing mode with a vertical resolution of up to 7.5 m and a maximum temporal resolution of 1 s.

3 Observations

3.1 Features inside the Arctic boundary layer clouds

During VERDI, thirteen measurement flights were performed around Inuvik and above the Beaufort Sea which was partly covered with ice. The probed super-cooled liquid water clouds were primarily observed after 8 May 2012. Before that time only mixed phase clouds, occasionally including with glaciated hydrometeors as large as 6 mm, were encountered during the observations.

The flight path of Flight 11 on 15 May 2012, is shown in Fig. 1, where a cloud layer was observed between 69.8° and 70.5° latitude (marked by the red line) in an altitude interval between 630 and 1060 m above sea level. Figure 2 shows profiles of different meteorological and microphysical parameters of this cloud. The cloud top as marked by the dashed line was at an altitude of 990 m. The layer directly above the dashed line (from 990 to 1060 m) is denoted as the transition zone in the following. Here the temperature T increased rapidly from 268 K to 271 K. The relative humidity RH inside the cloud was around 100 % and above the cloud top RH declined to values around 80 %. Thus, the cloud is capped by a layer of warmer and drier air which is typical for stratocumulus. The droplet number concentrations N, measured by the CDP, reveal constant values around 70 cm^{-3} almost independently of height. The liquid water content LWC (as derived from the measured droplet SDs), increased with altitude inside the cloud. Both, constant N and LWC concurrently increasing as function of height are typical for liquid water clouds generated by adiabatic lifting/cooling. The calculated adiabatic LWC is indicated by the dash-dotted line in Panel (d) of Fig. 2. While the measured and calculated LWCs are fairly close within the lowest 90 m of the cloud the influence of the entrainment processes becomes increasingly evident by the deviations between the two in the upper regions of the cloud.

To further characterize the atmospheric stability inside the cloud, the liquid water potential temperature θ_l (according to Stevens, 2005) is calculated. θ_l represents the potential temperature attained by evaporating all the liquid water in an air parcel through

reversible wet adiabatic descent (Betts, 1973) and is defined as:

$$\theta_l \approx \theta \exp\left(\frac{-\mathrm{LWC} L_\mathrm{v}}{c_p T}\right). \quad (1)$$

Here θ represents the potential temperature for dry air in Kelvin, LWC [in $\mathrm{g\,m}^{-3}$] is the mass of liquid water, while the latent heat of vaporization is denoted as L_v [in $\mathrm{J\,kg}^{-1}\,\mathrm{K}^{-1}$], the heat capacity as c_p [in $\mathrm{J\,kg}^{-1}\,\mathrm{K}^{-1}$] and the temperature as T following Stevens (2005). In Panel (e) of Fig. 2 the liquid water potential temperature θ_l exhibits a continuous increase with altitude, which clearly indicates stable atmospheric conditions inside the cloud. In the following, the microphysical measurements from Flight 11 on 15 May are described in detail for the layer inside the cloud (630–990 m) and in the transition zone (990–1060 m) directly above.

The studied cloud mainly consists of super-cooled liquid water droplets. Only a few ice particles, mostly needles, with a number concentration of 7.5×10^{-4} cm^{-1}, were occasionally detected by the CIPgs instrument between altitudes of 630 to 990 m. Figure 3 shows a time series of the aerosol number concentration (Fig. 3a) and the droplet geometric mean diameter (Fig. 3b). Inside the cloud and during ascent between 20:08 and 20:22 UTC the droplet geometric mean diameter increased with altitude while the aerosol number concentration decreased.

The increasing size of the cloud droplets is also obvious in Fig. 4a–c where the narrow and monomodal SDs from different altitudes are displayed. The modal droplet diameter grows continuously from 12 to 20 µm with altitude. Calculations for diffusional droplet growth, which are based on the set of four differential equations given in Pruppacher and Klett (2010) including released latent heat conduction to the air and back to the droplets, provide the necessary time for the droplets to grow from 12 µm to 20 µm under the given ambient conditions. Assuming values for the relative humidity of 100.15 %, 100.10 %, and 100.08 % the calculations indicate growth times of 7, 15 and 37 min, respectively, which is well within the range of lifetimes for such clouds or cloud fragments.

The SDs monomodal shape and the monotonic increase of their size peak is comparable with observations by Lawson et al. (2001), who explained their appearance by adiabatic ascent of in-cloud air. As shown in Fig. 2d, deviations between the measurements and the expected adiabatic LWC due to an adiabatic ascent are obvious and indicate that the in-cloud air does not experience fully adiabatic conditions in our case. Continuous ascent throughout a certain altitude range implies averaging over an extended section of the linear flight path inside the cloud. This may have contributed to the deviations as it differs from a real vertical profile above one specific location.

Inside the transition zone at the cloud top, bimodal SDs with a second mode around 10 µm are observed, as can be seen in Fig. 5c. This phenomenon was encountered only in the transition zone of the cloud during three VERDI flights (Flight 9 on 10 May, Flight 11 on 15 May and Flight 13 on 17 May). For the other flights in liquid water clouds only an increase of the droplet size diameter with altitude was found. The reason why during these flights no bimodal SDs were detected in the transition zone can be explained by the flight profile, which the aircraft conducted. The bimodal SDs only were observable (1) when the aircraft spent at least 1 s (~ 70 m) in the transition zone, or (2) when the plane slowly enough approached the top from below inside the cloud or entering the cloud coming from above. Often the aircraft crossed the relevant highest cloud level too fast for the acquisition of a size distribution with good counting statistics in each mode.

The SD shown in Fig. 5b was detected inside the cloud at an altitude of 1004 m and shows a monomodal shape similar to Fig. 4. To distinguish both modes, in the following the mode at larger sizes (20 µm) will be labeled as Mode 1 and the one at smaller sizes is denoted as Mode 2. Figure 5a indicates that during Flight 11 several flight sequences with bimodal SDs were detected between 20:22:00 and 20:27:00 UTC when the aircraft flew through the transition zone of the cloud.

Besides the cloud droplets, also aerosol particles were measured during the VERDI campaign by using the Sky-OPC and AMALi. Figure 6 shows two examples of AMALi backscatter plots from two different flights and for times when the aircraft emerged

from the cloud top and turned around to fly longer stretches above and in the vicinity of the cloud parts which was in-situ sampled directly before. The total attenuated backscatter signal is shown, which consists of light scattered from the cloud particles as well as the air molecules (as a background contribution). The coarse color scale provides a rough estimate of the intensity of the scattering. It is normalized with respect to the values between 2100 m and 2400 m, assuming a low and homogeneous aerosol concentration at that altitude. The upper panel shows the backscatter signal from the penetrated boundary layer cloud during Flight 11. The backscatter signal does not show a distinct pattern above the cloud, only a very slight decrease with altitude. This decrease can at least partly be attributed to Rayleigh scattering from air molecules, leaving only very little variation in aerosol backscatter. Any aerosol visible for AMALi can therefore be assumed to be distributed uniformly in space supporting the assumption of arctic background aerosol. In order to highlight the differences compared to other atmospheric conditions, the lower panel shows the data of Flight 10 on 5 May. During this flight an optically thick aerosol layer (OD = 0.02 ± 0.005 assuming a lidar ratio of 40 sr) is discernible above the cloud. This layer probably cannot be classified as Arctic background Aerosol. HYSPLIT reanalysis trajectories over 72 h (see http://ready.arl.noaa.gov/HYSPLIT.php) indicate that the aerosol originates from Yukon Territories and Alaska in an altitude range between 500 and 1500 m.

Every time during Flight 11, when the ascending aircraft penetrated the cloud top, the number concentration of the aerosol particles in a size region between 250 nm < D_p < 1 µm increased from 0.7 (±0.08) cm^{-3} up to 7.5 (± 0.02) cm^{-3}. Considering the clear Arctic atmosphere with generally low number densities in the measured size range this represents a significant difference. Figure 3a shows this increase in the aerosol number concentration at 20:25:00 and 20:31:30 UTC. Aerosol particle size distributions from the OPC measurements are shown in Fig. 7. In order to provide a comparison with a typical clean atmosphere encountered during VERDI, a Sky-OPC SD from Flight 10 on 14 May is added and from the error bars (based on counting statistics) the range of variability can be seen. The aerosol number concentration above the cloud, particu-

larly in the small size regions with 250 nm < D_p < 500 nm, is by a factor of about seven higher than inside the cloud. Unfortunately, for detecting particles smaller than 250 nm no instrument was available during the VERDI campaign. For this reason, the averaged dry Arctic background aerosol size distribution, which was measured as regional average by Lathem et al. (2013) with an Scanning Mobility Particle Sizer (SMPS), is adapted and also included in Fig. 7 for comparison.

In addition to the SMPS system Lathem et al. (2013) used a Cloud Condensation Nuclei Counter (CCNC) to determine the fraction of aerosol that can be activated to cloud droplets. They found an activation ratio of 0.52 (at 0.55 % internal supersaturation inside the instrument) which shows that approximately half of the measured Cloud Nuclei (CN) was activated.

Despite the uncertainties inherent in a comparison of measurements which were four years apart, this juxtaposition shows that the aerosol concentrations match quite well. In particular the background aerosol particles measured above the cloud during VERDI does not show higher number densities than that reported by Lathem et al. (2013). Therefore, the detected aerosol above the cloud on 25 May 2012, might well be considered as dry Arctic background aerosol which seems to be continuously present in this region.

3.2 Spatial distribution of the droplets from the bimodal size distributions

To exclude the possibility that the bimodal SDs are result of a sampling artifact caused by time-averaging over spatially separated particle populations with different size modes, the PbP data from the CDP were examined. In this way the sizes and the exact detection times for consecutive single detected particles become available. Figure 8 shows a plot based on PbP analysis for data collected during a 4.5 s period (i.e. a flight segment of roughly 315 m length) from Flight 11, which is the particular period where the bimodal SD shown in Fig. 5c was observed. Figure 8 displays the two size modes separated by the dashed line. Mode 1 covers particle diameters around 20 µm and Mode 2 those around 10 µm. Overall, 1023 particles were recorded in this period.

The time gaps, where no consecutive particles are displayed, result from the limited buffer capacity and transmission speed (max. 256 particles in one second) of the PbP recording. The continuous PbP-records in Fig. 8 are roughly 0.3 s long and correspond to about 20 m of flight distance within the cloud. To illustrate the mixing state of both modes, the detected particles are labeled with two colors. The red color dots represent particles where the previously detected particle was from the same size mode. The black dots mark particles where the previously detected particle is assigned to the other mode. If the aircraft had moved through one patch of air containing only Mode 1 particles (like in the SDs of Fig. 4) and afterwards through a different air parcel with mostly droplets from Mode 2 – for example because the two parcels were from different entrainment filaments –, then a bimodal SD might result from data averaging over a sufficiently long flight path stretch. In this case the PbP "arrival time analysis", however, would have revealed such effects. To investigate the mixing of the two modes on such scales, a statistical approach is used by comparing the probabilities of black and red dots to those of an ideal mixing state where particles from any of the two modes are detected at random. The probability of detecting two successive particles from two different size modes in a fully random process is:

$$P_{12+21} = p_1 p_2 + p_2 p_1 = 2\,(p_1\,(1 - p_1)) = 2p_1 - 2p_1^2, \quad (2)$$

with p_1 and p_2 designating the occurrence rates (i.e. the probabilities) of particles from Mode 1 and Mode 2 and with $p_1 + p_2 = 1$. Figure 9 displays P_{12+21} from Eq. (1) as black line.

Consider as example that 100 particles were successively detected with 60 (abscissa = 0.6) originating from Mode 2 and 40 from Mode 1. In this case the probability of having two random consecutive particles and finding them in different modes is in theory 48 %. For the measured example, however, it was 44.7 % and in this case, the bimodal SD shown in Fig. 8 is close to a uniform distribution (see Fig. 9). The mean interarrival time between the individual particles is 1.45 milliseconds. Therefore, with

an aircraft speed of 70 m s^{-1}, the mean distance between two detected particles is roughly 10 cm. It can be concluded that within this detection rate, limited by the nearly one-dimensional sample volume of the instrument, both size modes are well mixed on the decimeter scale.

Further bimodal SDs from Flight 9 and Flight 16 were examined and also integrated in Fig. 9. In summary, four bimodal SDs (marked by circles) seem to result from well mixed air parcels. For the other three bimodal SDs, the agreement with the uniform distribution is less pronounced which suggests clustering of particles in each single mode (on sub-meter scale). In these clustered cases, the cloud droplets essentially were sampled from two disjoint particle ensembles.

4 Theoretical considerations and modeling

We first consider the possibility that the entrainment of dry aerosols from the free atmosphere might lead to cloud droplet nucleation, and the formation of the second mode in the SD (around 10 µm). This process was invoked by Lawson et al. (2001) to explain the bimodal SDs in their observations.

Isobaric mixing can lead to the necessary supersaturation for condensation if the saturation-vapor-pressure curve is sufficiently nonlinear over the temperature range relevant for the mixing. Figure 10 shows the saturation-vapor-pressure curve, in comparison with the studied case from the flight of 15 May 2012. The saturation-vapor-pressure curve is almost linear in the range covered by the measurements, indicating that the condensation of new droplets in the mixing is very unlikely. In this section we provide an explanation for the observed bimodal SDs, based on model results. The main assumption is that the bimodal SDs are a result of the turbulent mixing dynamics at the stratocumulus top. This premise is supported by the fact that all bimodal SDs were observed close to the cloud top, in contrast to the clear monomodal SDs inside the cloud. Here we use direct numerical simulations, DNS, to show how the turbulent

mixing dynamics at the stratocumulus top can generate a bimodal SD, similar to the distribution observed in the measurements.

The two main mechanisms for turbulent mixing in stratocumulus are infrared radiative and evaporative cooling. Close to the cloud top infrared radiation cools parcels that "fall back down into" the cloud, initiating turbulence and mixing. Turbulent mixing entrains dry air from the free atmosphere above the cloud, causing the evaporation of cloud droplets. The evaporative cooling involved in this process can in turn considerably enhance the turbulent mixing at the cloud top, depending on the thermodynamically properties of the cloud and adjacent free atmosphere. In some cases a horizontal wind shear can be strong enough to contribute or even dominate the mixing process.

As next step, three-dimensional numerical simulations were used in order to show that mixing and evaporation can explain the bimodal SDs. We performed numerical simulations of a mixing layer that is driven by radiative and evaporative cooling, thus resembling the stratocumulus top. In this study we focus on the small-scale mixing dynamics, and we neglect other cloud processes like microphysics, surface fluxes, shear or rain. Mellado (2010) and de Lozar and Mellado (2013a) showed that simulations of such a simplified configuration are a valid approach for the investigations of cloud-top mixing. DNS were applied for the calculations because they provide a faithful representation of the mixing, even at the smallest resolved scales. In our calculations we simulate scales from a Kolmogorov length η = 15 cm to an integral length scale of 200 m, thus capturing the relevant scales for mixing. The set of governing equations is based on the one-moment bulk scheme described in de Lozar and Mellado (2013b). The equations are further simplified by linearizing the buoyancy and the saturation-vapor-pressure functions around a reference state. The resulting formulation is equivalent to the one presented by Bretheron (1987), and it will be presented in a forthcoming manuscript. In this approximation the saturation-vapor-pressure function is linear, and therefore the isobaric condensation mixing is neglected. The long-wave radiation model is a one dimensional model, that assumes that radiation only propagates in the vertical

direction (Larson et al., 2007). We neglect the short-wave radiation due to its small warming contribution in Arctic clouds.

The thermodynamic parameters used in the simulation are based on the measurements from the flight of 15 May 2012: LWC = 0.25 g kg^{-1}, Total Water Content TWC = 3.15 g kg^{-1}, T = 268.15 K and Θ_l = 275.2 K in the cloud layer; and TWC = 2.4 g kg^{-1}, T = 272.65 K, RH = 59 % and Θ_l = 280.5 K in the dry air layer above the cloud. The atmospheric pressure is 905 hPa. The cloud-top radiative cooling, F_0 = 60 W m^{-2}, matches the data from the instruments on board the POLAR 5, and an extinction length was chosen to λ = 15 µm (see Larson (2007) and de Lozar and Mellado (2013a) for an explanation of the radiation parameters). The simulation runs for 12 min and the largest length scale of turbulence is 200 m. The grid employed in the numerical simulations contains 1024^3 points, the width of the simulation domain is 270 m and the resulting grid spacing in the region of interest is 26 cm.

Figure 11 shows a vertical cross section from our simulations, in which the liquid water density ranges from 0.0 g kg^{-1} (blue) to 0.325 g kg^{-1} (white). Turbulence and mixing are evident in the transition zone between the cloud and free dry atmosphere, as it is typical for stratocumulus clouds. In the transition zone the entrained air concentrates on some regions that are indicated by red squares in Fig. 11. We specify these regions as holes, in analogy to the liquid free regions observed by Gerber et al. (2005) in some tropical clouds. In comparison to the previously observed holes, the holes in our simulations contain more liquid water and stay closer to the cloud top. These differences are explained by the relatively high humidity of the free atmosphere measured in the flight of 15 May 2012 (RH = 59 %) above the cloud. The potential for evaporation is lower and therefore it is not surprising that some liquid water remains in the holes after the mixing process. We also see that the liquid water concentration in Artic clouds is usually lower than in tropical clouds. Given the combination of low cloud water concentration and still enough water vapor in the free atmosphere, the evaporative cooling is expected to be low. As a consequence the air in the holes is mostly positively buoyant, and the holes have a tendency to remain close to the cloud top.

Our hypothesis is that the bimodal SDs shown in Fig. 5c are a result of the mixing within the holes and for testing we simulated the SD that an aircraft would measure in our model, when flying close to the cloud top (black line in Fig. 11). The mean diameter of the droplets in each grid box was calculated using the liquid water from the simulations and a droplet number concentration N = 70 cm^{-3} as measured e.g. in Fig. 2. For the last 70 m of the simulated plane trajectory (including the big hole highlighted by the bounding box) the size distribution shows a bimodal shape (see Fig. 13) which qualitatively agrees with Fig. 5c. Even though the minima between the two modes in the size distributions are 4 µm apart and the number concentrations of the large droplet mode are quite different the SD are similar enough to suggest that the evaporation of droplets in the holes causes the bimodality.

The second mode in the SDs in the simulations can be explained if we assume that the large-scale dynamics of each hole are dominated by a single large eddy, while the rapid mixing inside the holes is due to much smaller turbulent eddies. The time scale of the large eddy determines the mixing and composition inside a hole, defining a typical droplet diameter: large eddies are able to capture large quantities of dry air resulting in a small typical droplet diameter, while smaller eddies are characterized by larger droplet diameters. This picture seems to be consistent with the composition of the holes in Figures 11 and 12. Most likely the second mode with the smaller droplets in the SD represents the typical droplet diameter of the hole in a bounding box, whereas the first, larger droplet mode corresponds to cloud droplets that have not yet been mixed.

5 Conclusions

The VERDI campaign was performed to study microphysical and radiative properties of Arctic boundary layer clouds in the Beaufort Sea area. Microphysical measurements by Lawson et al. (2001) show the occurrence of monomodal and bimodal SDs caused by adiabatic ascent and activation of new CCN, which were entrained. In the VERDI

campaign similar SDs were observed in boundary layer clouds during three flights and inside the analyzed cloud monomodal SDs were found. Measurements of the LWC indicate deviations from adiabatic conditions and, therefore, entrainment processes at the top of the penetrated cloud play a role. LiDAR and aerosol instruments above the cloud layers show well mixed aerosol particle population which can be classified as dry Arctic background aerosol. In the cloud transition zone at altitudes between 990 and 1060 m a change from monomodal SDs towards bimodal SDs was observed. A method adopting particle-inter-arrival-times was applied to study the mixing progress between both droplet modes ultimately demonstrating that for four of seven bimodal SDs a nearly uniform mixing process prevailed. This means that an artifact due to time averaging over spatially separated particle population can be excluded on a decimeter scale. The other cases indicate a sampling from two disjoint particle ensembles.

The development of the second mode in the transition zone could in principle be explained (a) by activation/condensation of newly entrained CCN or (b) by evaporation processes. Condensation from isobaric mixing is only possible for configurations with large deviations in temperature and water vapor concentration. In the measurements the temperature variations between cloud and free atmosphere are so small that the saturation-vapor-pressure curve is almost linear in this range, making isobaric condensation of new droplets very unlikely. For this reason evaporation processes were examined in more detail by using a model simulation study. This model considered evaporative and radiative cooling and produces regions with concentrated entrained air. The results of the simulation study are in qualitative agreement with the measurements. Turbulent entrainment eddies seem to be responsible for the development process of the second size mode (10 µm) whereas the first size mode (20 µm) represents droplets that have not yet mixed with drier air from above.

In conclusion, inside the transition zone of the observed boundary layer clouds we detected bimodal SDs where the second (smaller) size mode seems to be a result from eddy driven in-mixing of drier air with subsequent evaporation. To analyze this phenomenon in a higher resolution a holographic instrument capable of detecting par-

ticles in a sample volume of a few cm^3 in a single snapshot (Spuler and Fugal, 2011) will allow to investigate still smaller mixing scales of both size modes. Also new imaging remote sensing techniques as presented by Bierwirth et al. (2013) will help to identify the horizontal variability of such type of clouds and help to quantifiy eddy driven mixing processes.

Acknowledgements. This work was supported by internal sources of the Max Planck Society with additional funds for the execution of the research flights be the Alfred Wegener Institute for Polar Research (Bremerhaven, Germany). We thank the Aurora Research Center for the support and the hospitality in Inuvik. The support by the electrical engineers Wilhelm Schneider and Christian von Glahn is very much appreciated. We particularly thank the scientists, the pilots and the crew of the POLAR 5 and all other VERDI participants and contributors. Computational time was provided by the Jülich Supercomputing Centre.

References

Avramov, A., Ackerman, A. S., Fridlind, A. M., van Diedenhoven, B., Botta, G., Aydin, K., Verlinde, J., Korolev, A. V., Strapp, J. W., McFarquhar, G. M., Jackson, R., Brooks, S. D., Glen, A., and Wolde, M.: Toward ice formation closure in Arctic mixed-phase boundary layer clouds during ISDAC, J. Geophys. Res.-Atmos., 116, D00T08, doi:10.1029/2011jd015910, 2011.

Betts, A. K.: Non-precipitating cumulus convection and its parameterization, Q. J. Roy. Meteor. Soc., 99, 178–196, 1973.

Bierwirth, E., Ehrlich, A., Wendisch, M., Gayet, J.-F., Gourbeyre, C., Dupuy, R., Herber, A., Neuber, R., and Lampert, A.: Optical thickness and effective radius of Arctic boundary-layer clouds retrieved from airborne nadir and imaging spectrometry, Atmos. Meas. Tech., 6, 1189–1200, doi:10.5194/amt-6-1189-2013, 2013.

Bretheron, C. S.: A theory for nonprecipitating moist convection between 2 parallel plates .1. Thermodynamics and linear solutions, J. Atmos. Sci., 44, 1809–1827, 1987.

Curry, J. A., Rossow, W. B., Randall, D., and Schramm, J. M.: Overview of Arctic cloud and radiation characteristics, J. Climate, 9, 1731–1764, 1996.

Curry, J. A., Hobbs, P. V., King, M. D., Randall, D. A., Minnis, P., Isaac, G. A., Pinto, J. O., Uttal, T., Bucholtz, A., Cripe, D. G., Gerber, H., Fairall, C. W., Garrett, T. J., Hudson, J.,

Intrieri, J. M., Jakob, C., Jensen, T., Lawson, P., Marcotte, D., Nguyen, L., Pilewskie, P., Rangno, A., Rogers, D. C., Strawbridge, K. B., Valero, F. P. J., Williams, A. G., and Wylie, D.: FIRE Arctic Clouds Experiment, B. Am. Meteorol. Soc., 81, 5–29, 1999.

de Lozar, A. and Mellado, J. P.: Cloud droplets in a bulk formulation and its application to buoyancy reversal instability, Q. J. Roy. Meteor. Soc., doi:10.1002/qj.2234, 2013a.

de Lozar, A. and Mellado, J. P.: Direct numerical simulations of a smoke cloud–top mixing layer as a model for stratocumuli, J. Atmos. Sci., 70, 2356–2375, doi:10.1175/jas-d-12-0333.1, 2013b.

Ehrlich, A., Wendisch, M., Bierwirth, E., Herber, A., and Schwarzenböck, A.: Ice crystal shape effects on solar radiative properties of Arctic mixed-phase clouds – dependence on microphysical properties, Atmos. Res., 88, 266–276, 2008a.

Ehrlich, A., Bierwirth, E., Wendisch, M., Gayet, J.-F., Mioche, G., Lampert, A., and Heintzenberg, J.: Cloud phase identification of Arctic boundary-layer clouds from airborne spectral reflection measurements: test of three approaches, Atmos. Chem. Phys., 8, 7493–7505, doi:10.5194/acp-8-7493-2008, 2008b.

Ehrlich, A., Wendisch, M., Bierwirth, E., Gayet, J.-F., Mioche, G., Lampert, A., and Mayer, B.: Evidence of ice crystals at cloud top of Arctic boundary-layer mixed-phase clouds derived from airborne remote sensing, Atmos. Chem. Phys., 9, 9401–9416, doi:10.5194/acp-9-9401-2009, 2009.

Fan, J., Ovtchinnikov, M., Comstock, J. M., McFarlane, S. A., and Khain, A.: Ice formation in Arctic mixed-phase clouds: insights from a 3-D cloud-resolving model with size-resolved aerosol and cloud microphysics, J. Geophys. Res., 114, D04205, doi:10.1029/2008JD010782, 2009.

Gerber, H., Frick, G., Malinowski, S. P., Brenguier, J. L., and Burnet, F.: Holes and entrainment in stratocumulus, J. Atmos. Sci., 62, 443–459„ 2005.

Hansen, J., Ruedy, R., Sato, M., and Lo, K.: Global surface temperature change, Rev. Geophys., 48, RG4004, doi:10.1029/2010RG000345, 2010.

Huebert, B. J., Howell, S. G., Covert, D., Bertram, T., Clarke, A., Anderson, J. R., Lafleur, B. G., Seebaugh, W. R., Wilson, J. C., Gesler, D., Blomquist, B., and Fox, J.: PELTI: measuring the Passing Efficiency of an Airborne Low Turbulence Aerosol Inlet, Aerosol Sci. Tech., 38, 803–826, 2004.

Jacob, D. J., Crawford, J. H., Maring, H., Clarke, A. D., Dibb, J. E., Emmons, L. K., Ferrare, R. A., Hostetler, C. A., Russell, P. B., Singh, H. B., Thompson, A. M., Shaw, G. E., McCauley, E., Pederson, J. R., and Fisher, J. A.: The Arctic Research of the Composition of the Troposphere

from Aircraft and Satellites (ARCTAS) mission: design, execution, and first results, Atmos. Chem. Phys., 10, 5191–5212, doi:10.5194/acp-10-5191-2010, 2010.

Jensen, E. J., Lawson, P., Baker, B., Pilson, B., Mo, Q., Heymsfield, A. J., Bansemer, A., Bui, T. P., McGill, M., Hlavka, D., Heymsfield, G., Platnick, S., Arnold, G. T., and Tanelli, S.: On the importance of small ice crystals in tropical anvil cirrus, Atmos. Chem. Phys., 9, 5519–5537, doi:10.5194/acp-9-5519-2009, 2009.

Kay, J. E., L'Ecuyer, T., Gettelman, A., Stephens, G., and O'Dell, C.: The contribution of cloud and radiation anomalies to the 2007 Arctic sea ice extent minimum, Geophys. Res. Lett., 35, 5, L08503, doi:10.1029/2008GL033451, 2008.

Korolev, A. V.: Reconstruction of the sizes of spherical particles from their shadow images, Part I: Theoretical considerations, J. Atmos. Ocean. Technol., 24, 376–389, 2007.

Korolev, A. V., Emery, E. F., Strapp, J. W., Cober, S. G., Isaac, G. A., Wasey, M., and Marcotte, D.: Small ice particles in tropospheric clouds: fact or artifact? Airborne icing instrumentation evaluation experiment, B. Am. Meteorol. Soc., 92, 967–973, 2011.

Lance, S., Brock, C. A., Rogers, D., and Gordon, J. A.: Water droplet calibration of the Cloud Droplet Probe (CDP) and in-flight performance in liquid, ice and mixed-phase clouds during ARCPAC, Atmos. Meas. Tech., 3, 1683–1706, doi:10.5194/amt-3-1683-2010, 2010.

Larson, V. E., Kotenberg, K. E., and Wood, N. B.: An analytic longwave radiation formula for liquid layer clouds, Mon. Weather Rev., 135, 689–699, 2007.

Lathem, T. L., Beyersdorf, A. J., Thornhill, K. L., Winstead, E. L., Cubison, M. J., Hecobian, A., Jimenez, J. L., Weber, R. J., Anderson, B. E., and Nenes, A.: Analysis of CCN activity of Arctic aerosol and Canadian biomass burning during summer 2008, Atmos. Chem. Phys., 13, 2735–2756, doi:10.5194/acp-13-2735-2013, 2013.

Lawson, R. P., Baker, B. A., and Schmitt, C. G.: An overview of microphysical properties of Arctic clouds observed in May and July 1998 during FIRE ACE, J. Geophys. Res., 106, 14989–915014, 2001.

Lemke, P., Ren, J., Alley, R. B., Allison, I., Carrasco, J., Flato, G., Fujii, Y., Kaser, G., Mote, P., Thomas, R. H., and Zhang, T.: Observations: changes in Snow, Ice and Frozen Ground, in: Climate Change 2007: The Physical Science Basis. Contribution of Working Group I to the Fourth Assessment Report of the Intergovernmental Panel on Climate Change, edited by: Solomon, S., Qin, D., Manning, M., Chen, Z., Marquis, M., Averyt, K. B., Tignor, M., and Miller, H. L., Cambridge University Press, Cambridge, UK and New York, NY, USA., 2007.

Lihavainen, H., Kerminen, V.-M., and Remer, L. A.: Aerosol-cloud interaction determined by both in situ and satellite data over a northern high-latitude site, Atmos. Chem. Phys., 10, 10987–10995, doi:10.5194/acp-10-10987-2010, 2010.

Mellado, J. P.: The evaporatively driven cloud–top mixing layer, J. Fluid Mech., 660, 5–36, 2010.

Morrison, H., Pinto, J. O., Curry, J. A., and McFarquhar, G. M.: Sensitivity of modelled arctic mixed-phase stratocumulus to cloud condensation and ice nuclei over regionally varying surface conditions, J. Geophys. Res., 113, D05203, doi:10.1029/2007JD008729, 2008.

Palm, S. P., Strey, S. T., Spinhirne, J., and Markus, T.: Influence of Arctic sea ice extent on polar cloud fraction and vertical structure and implications for regional climate, J. Geophys. Res., 115, D21209, doi:10.1029/2010JD013900, 2010.

Perovich, D. K., Andreas, E. L., Curry, J. A., Eiken, H., Fairall, C. W., Grenfell, T. C., Guest, P. S., Intrieri, J., Kadki, D., Lindsay, R. W., McPhee, M. G., Morison, J., Moritz, R. E., Paulson, C. A., Pegau, W. S., Persson, P. O. G., Pinkel, R., Richter-Menge, J. A., Stanton, T., Stern, H., Sturm, M., Tucker, W. B., and Uttal, T.: Year in ice gives climate insights, EOS, 80, 481–492, 2000.

Perovich, D. K., Richter-Menge, J. A., Jones, K. F., and Light, B.: Sunlight, water, and ice: extreme Arctic sea ice melt during the summer of 2007, Geophys. Res. Lett., 35, 2008.

Pettersen, S.: On the causes and the forecasting of the California fog, B. Am. Meteorol. Soc., 19, 49–55, 1938.

Platnick, S.: Vertical photon transport in cloud remote sensing problems, J. Geophys. Res., 105, 22919–22935, 2000.

Pruppacher, H. R. and Klett, J. D.: Microphysics of Clouds and Precipitation, Springer, Dordrecht, Heidelberg, London, New York, 954 pp., 2010.

Schweiger, A. J. and Lindsay, R. W.: Relationships between Arctic sea ice and clouds during autumn, J. Climate, 21, 4799–4810, 2008.

Shupe, M. D. and Intieri, J. M.: Cloud radiative forcing of the Arctic surface: the influence of cloud properties, surface albedo, and solar angle, J. Climate, 17, 616–628, 2004.

Siems, S. T. and Bretheron, C. S.: A numerical investigation of cloud-top entrainment instability and related experiments, Q. J. Roy. Meteor. Soc., 118, 787–818, 1992.

Spuler, S. M. and Fugal, J.: Design of an in-line, digital holographic imaging system for airborne measurement of clouds, Appl. Optics, 50, 1405–1412, 2011.

Stevens, B.: Atmospheric moist convection, Annu. Rev. Earth Pl. Sc., 33, 605–643, 2005.

Struthers, H., Ekman, A. M. L., Glantz, P., Iversen, T., Kirkevåg, A., Mårtensson, E. M., Seland, Ø., and Nilsson, E. D.: The effect of sea ice loss on sea salt aerosol concentrations and the radiative balance in the Arctic, Atmos. Chem. Phys., 11, 3459–3477, doi:10.5194/acp-11-3459-2011, 2011.

Wendisch, M. and Brenquier, J.-L.: Airborne Measurements for Environmental Research: Methods and Instruments, Wiley-VCH Verlag GmbH & Co. KG, Weinheim, Germany, 655 pp., 2013.

Wendisch, M., Yang, P., and Ehrlich, A.: Amplified climate changes in the Arctic: Role of clouds and atmospheric radiation. Sitzungsberichte der Sächsischen Akademie der Wissenschaften zu Leipzig. Mathematisch-Naturwissenschaftliche Klasse, S. Hirzel Verlag, Stuttgart/Leipzig, 132, 1–34, 2013.

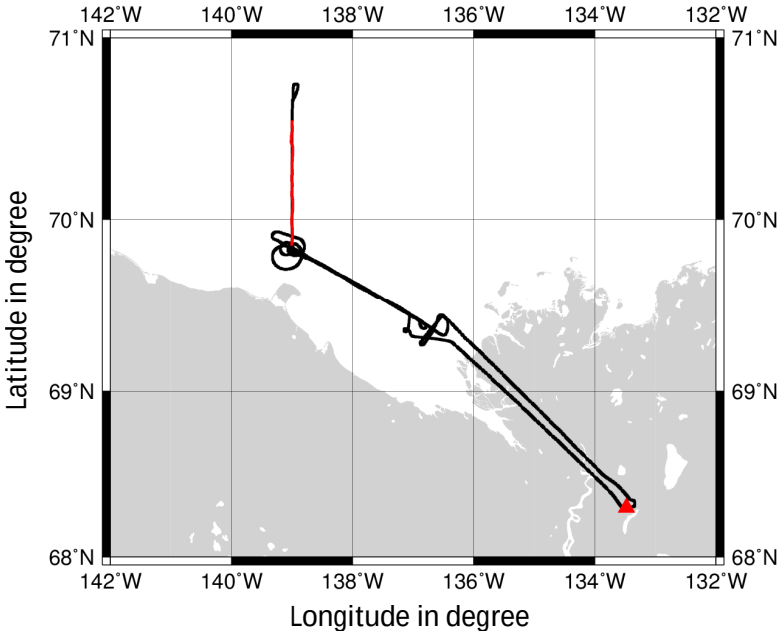

Figure 1. Track of Flight 11, performed on 15 May in the Northwest Territories of Canada and the Beaufort Sea. The triangle marks Inuvik airport and the red line shows the region where the boundary layer cloud was penetrated.

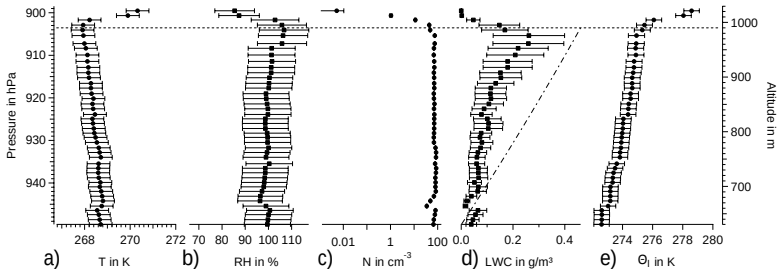

Figure 2. Altitude profiles inside the penetrated cloud during Flight 11 (20:05–20:25 UTC) on 15 May 2012. Gradients of temperature T and the relative humidity RH above 990 m indicate that the cloud is capped by a warmer and drier atmosphere. The droplet number concentration N is constant inside the cloud. LWC and the liquid water potential temperature Θ_l show an increase with altitude. The adiabatic LWC is indicated by the dash-dot line. The horizontal dashed line marks the beginning of the transition zone in an altitude of 990 m. Error bars for T and RH resulting from the uncertainty of the instruments. The errors for N are based on counting statistics and are very small. For LWC and Θ_l the error is calculated by error propagation.

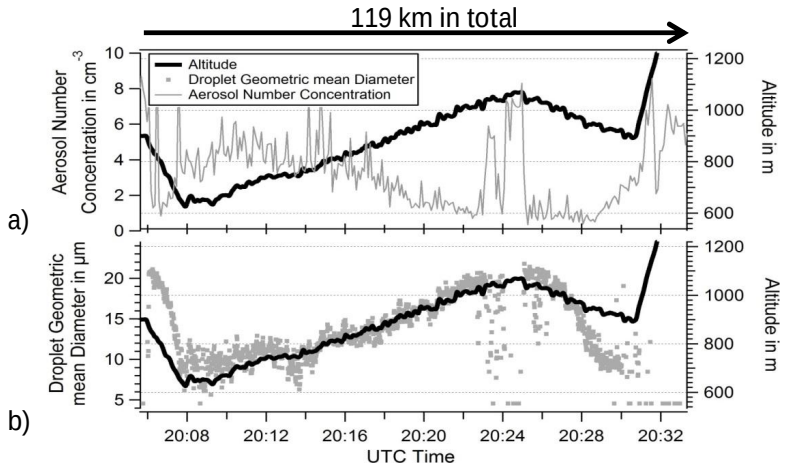

Figure 3. Time series of cloud in-situ measurements. Aerosol number concentration (**a**, grey line) and mean droplet diameter (**b**, grey dots) during Flight 11 on 15 May 2012. Flight altitude is indicated in both panels by a solid black line.

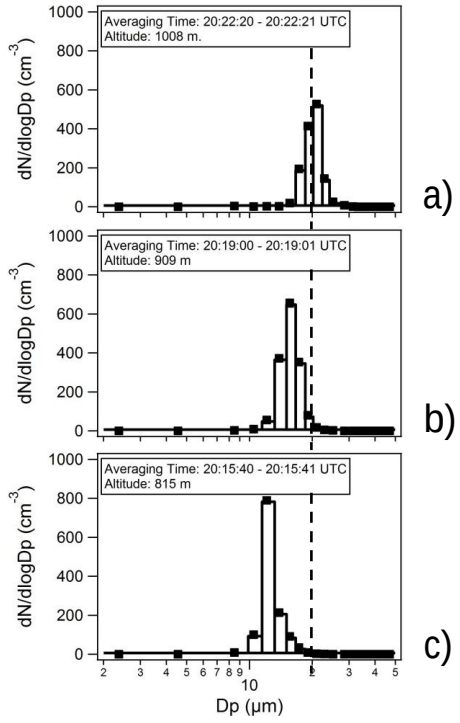

Figure 4. Monomodal SDs from Flight 11 on 15 May 2012. Note the linear scale of the ordinates. The dashed line marks the 20 µm diameter. A continuous increase of the droplet particle diameter with increasing altitude from **(c)** to **(a)** is shown.

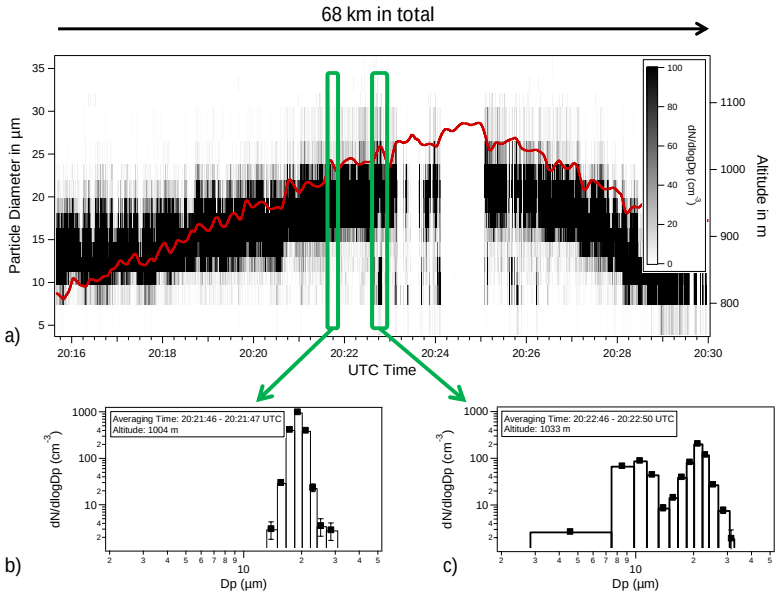

Figure 5. Upper panel: time series of measured cloud particle data from Flight 11 on 15 May 2012. The contour plot displays particle diameters over time. The greyscale describes the number concentration. The red line represents the flight altitude. Lower panel: two different SDs are shown. **(b)** was detected inside the cloud and **(c)** in the cloud's transition zone. Exclusively in the transition zone, SDs with two modes occur.

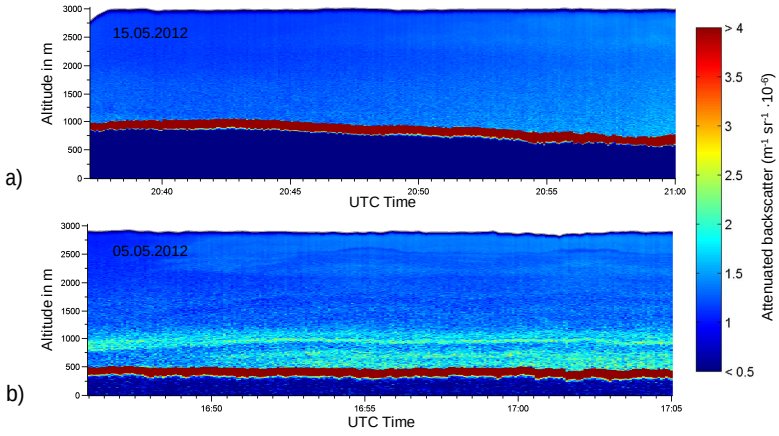

Figure 6. (a) AMALi backscatter signal from the studied boundary cloud layer in comparison with **(b)** a AMALi backscatter signal from a thick aerosol layer above a cloud.

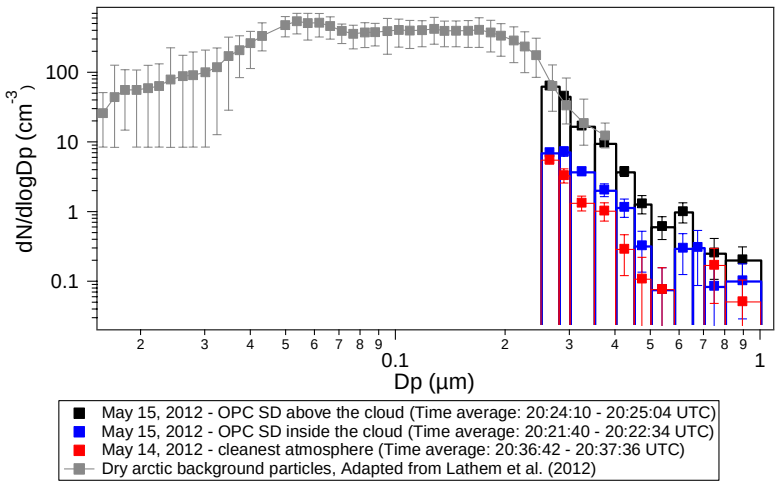

Figure 7. SDs of Flight 11 on 15 May 2012 in comparison with measurements during a clean atmospheric situation from Flight 10 on 14 May 2012. The error bars reflect the uncertainties due to the counting statistics while the width of the columns indicates the size bin limits. The assumed trend towards smaller sizes is shown by the adaption of the averaged dry Arctic background aerosol SD, measured by Lathem et al. (2012) using a SMPS system.

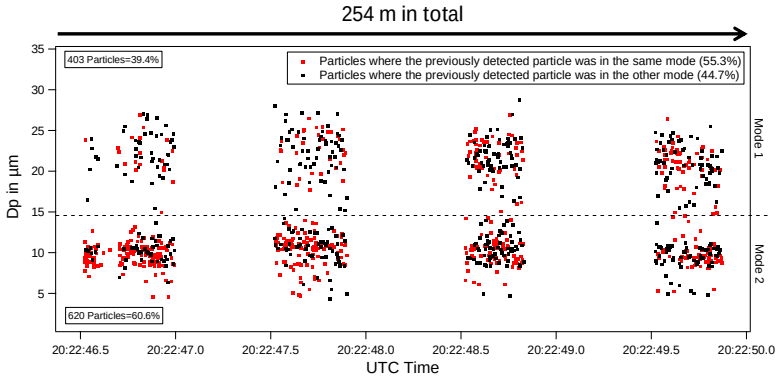

Figure 8. Fraction of Flight 11 on 15 May 2012. The detected particles are separated in Mode 1 and Mode 2. The red points mark particles where the previous detected particle was in the same mode. Black points mark particles where the previous detected particle was in the other size mode. More particles (60.6 %) were detected in Mode 2.

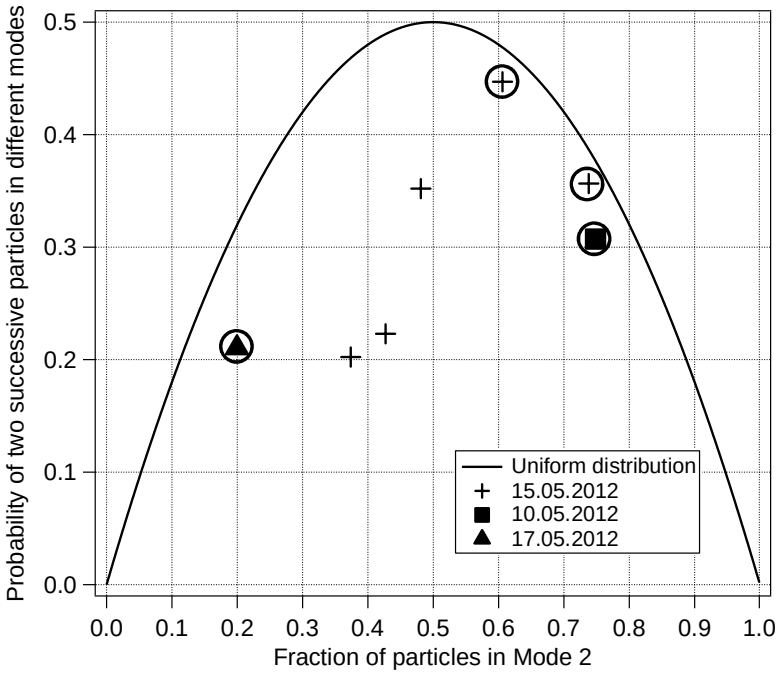

Figure 9. Evaluation of the bimodal SDs. The black line shows a uniform distribution between both size modes. The results from Fig. 8 (60.6 %, 44.7 %) indicate that the bimodal SD is close to an uniform distribution. All in all, four bimodal SDs show a good agreement with the uniform distribution (marked by circles). The agreement for the other bimodal SDs is weak.

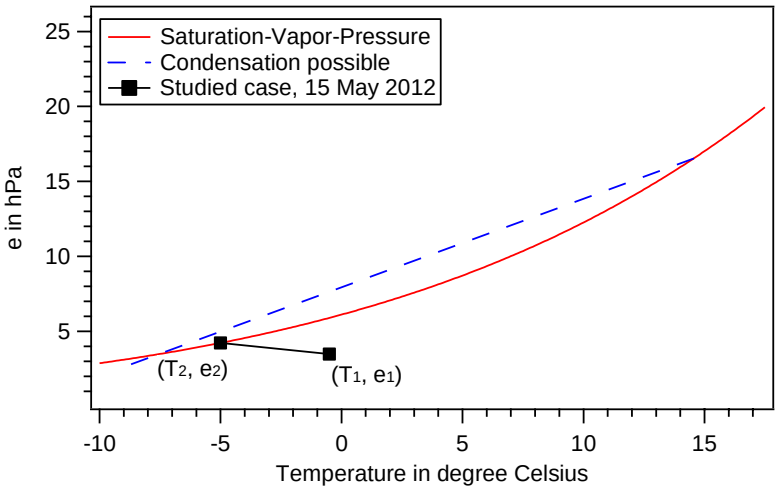

Figure 10. Isobaric mixing between a cloud and a dry air parcel. The studied case from 15 May 2012 is represented by the straight line. The thermodynamic parameters $T_1 = -0.5\,^{\circ}\mathrm{C}$, $\mathrm{RH}_1 = 59\,\%$, $e_1 = 3.5\,\mathrm{hPa}$ for dry air and $T_2 = -5\,^{\circ}\mathrm{C}$, $\mathrm{RH}_2 = 100\,\%$, $e_2 = 4.2\,\mathrm{hPa}$ inside the cloud are based on the measurements. Isobaric condensation occurs when in mixing of two parcels results in a composition that lays below the condensation line, due to the nonlinearity (or curvature) in the saturation-vapor-pressure function. The dashed line in the figure illustrates such a mixing process. However, the temperature range covered by our measurements (shown by the continuous line) is so small that the saturation-vapor-pressure is almost linear in this range. As a consequence, condensational mixing is very unlikely and cannot play an important role for generating the second mode in the bimodal SDs.

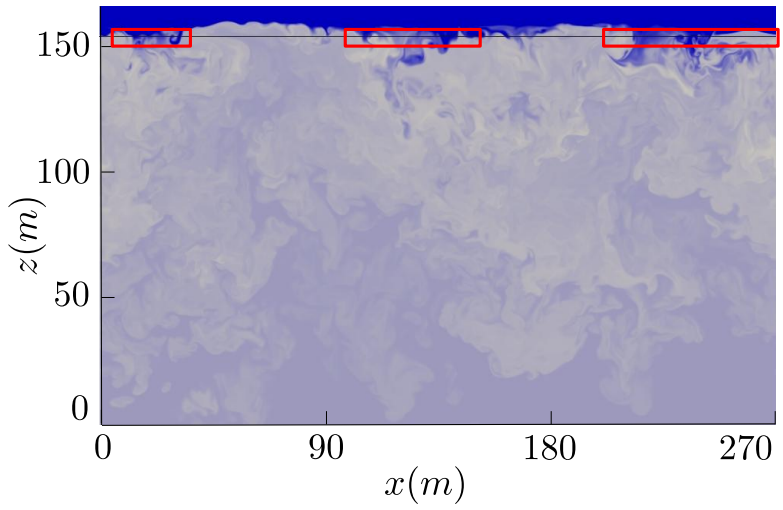

Figure 11. Vertical cross section of the simulated cloud liquid water. The black line indicates the trajectory of the simulated plane and the red rectangles mark the cloud holes. The color scale goes from 0.0 g kg^{-1} (blue) to 0.325 g kg^{-1} (white).

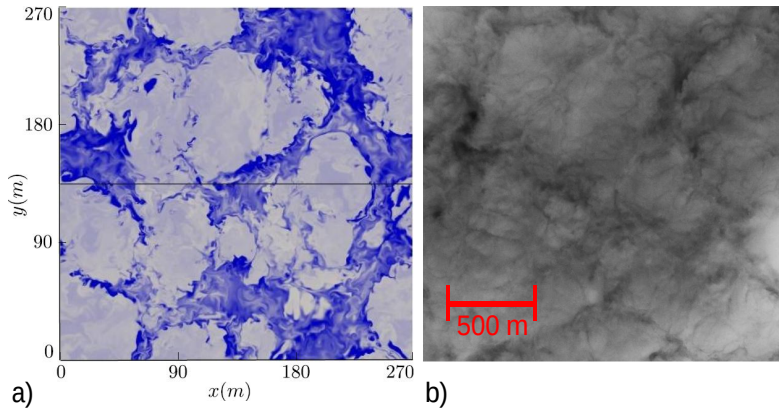

Figure 12. (a) Horizontal cross section of cloud liquid water. The simulated plane trajectory is given by the black line and the color coded scale is the same as in Fig. 11. **(b)** Picture, taken by a camera mounted at the fuselage of the aircraft, shows the top of a boundary layer cloud which was observed during Flight 11. The scale of **(a)** and **(b)** is different but a good qualitative agreement between the shape of the measured cloud and the shape of the simulated cloud liquid water can be seen.

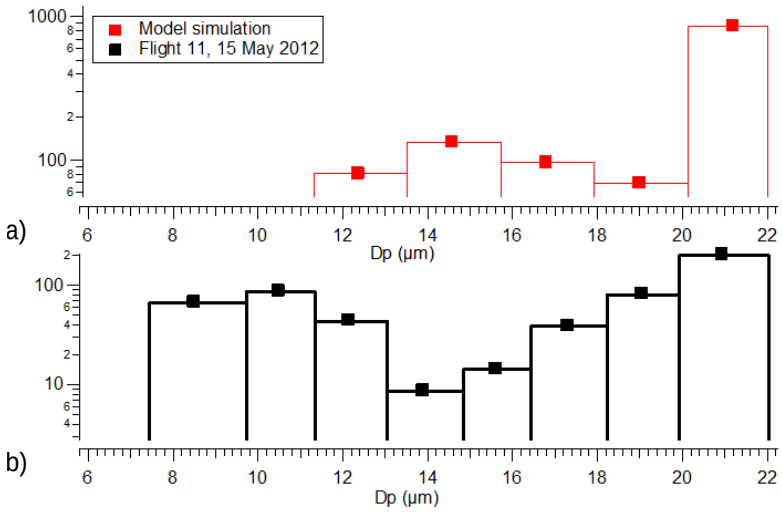

Figure 13. (a) A bimodal SD of the modeled droplets from the last 70 m of the simulated plane trajectory in comparison with **(b)** bimodal SD of the measured droplets during Flight 11 (see Fig. 5c).